

Wave-Induced Boundary Layer Separation in the Lee of the Medicine Bow Mountains. Part I: Observations*

JEFFREY R. FRENCH, SAMUEL J. HAIMOV, AND LARRY D. OOLMAN

Department of Atmospheric Science, University of Wyoming, Laramie, Wyoming

VANDA GRUBIŠIĆ⁺

National Center for Atmospheric Research,[#] Boulder, Colorado

STEFANO SERAFIN AND LUKAS STRAUSS

Department of Meteorology and Geophysics, University of Vienna, Vienna, Austria

(Manuscript received 16 December 2014, in final form 8 August 2015)

ABSTRACT

Two cases of mountain waves, rotors, and the associated turbulence in the lee of the Medicine Bow Mountains in southeastern Wyoming are investigated in a two-part study using aircraft observations and numerical simulations. In Part I, observations from in situ instruments and high-resolution cloud radar on board the University of Wyoming King Air aircraft are presented and analyzed. Measurements from the radar compose the first direct observations of wave-induced boundary layer separation.

The data from these two events show some striking similarities but also significant differences. In both cases, rotors were observed; yet one looks like a classical lee-wave rotor, while the other resembles an atmospheric hydraulic jump with midtropospheric gravity wave breaking aloft. High-resolution ($30 \times 30 \text{ m}^2$) dual-Doppler syntheses of the two-dimensional velocity fields in the vertical plane beneath the aircraft reveal the boundary layer separation, the scale and structure of the attendant rotors, and downslope windstorms. In the stronger of the two events, near-surface winds upwind of the boundary layer separation reached 35 m s^{-1} , and vertical winds were in excess of 10 m s^{-1} . Moderate to strong turbulence was observed within and downstream of these regions. In both cases, the rotor extended horizontally 5–10 km and vertically 2–2.5 km. Horizontal vorticity within the rotor zone reached 0.2 s^{-1} . Several subrotors from 500 to 1000 m in diameter were identified inside the main rotor in one of the cases.

Part II presents a modeling study and investigates the kinematic structure and the dynamic evolution of these two events.

 Denotes Open Access content.

* Supplemental information related to this paper is available at the Journals Online website: <http://dx.doi.org/10.1175/JAS-D-14-0376.s1>.

⁺ Additional affiliation: Department of Meteorology and Geophysics, University of Vienna, Vienna, Austria.

[#] The National Center for Atmospheric Research is sponsored by the National Science Foundation.

Corresponding author address: Samuel Haimov, University of Wyoming, Department 3038, 1000 E. University Ave., Laramie, WY 82071.
E-mail: haimov@uwyo.edu

1. Introduction

Terrain-induced internal gravity waves have been the subject of considerable research over the past several decades, primarily for the important role they play in association with damaging winds and severe turbulence both near the ground and aloft (Smith 1979; Baines 1995). One of the most turbulent phenomena associated with the terrain-induced gravity waves is an atmospheric rotor: an intense horizontal vortex with a complex internal structure that occurs underneath wave crests in the lee of the wave-generating mountain ridges. Rotors pose a serious threat to general aviation and can be important for the lofting

and transport of aerosols and contaminants (Doyle and Durran 2002).

The Terrain-Induced Rotor Experiment (T-REX; Grubišić et al. 2008) was conducted in Owens Valley, in the lee of Sierra Nevada, California, to collect high-resolution in situ and remotely sensed observations of this phenomenon, the spatial and temporal scales and variability of which represent a considerable hurdle to conventional, ground-based observational tools. Studies employing T-REX observations and measurements have been largely successful in confirming predictions of the theoretical and numerical studies, indicating that intense horizontal vorticity in rotors has its origin in the boundary layer vortex sheet that separates on the lee side of the mountain range because of the wave-induced boundary layer separation (Doyle et al. 2009; Cohn et al. 2011). The separation itself is induced by the adverse pressure gradient set up by the mountain wave. These studies, in particular, have successfully documented the complex internal structure of rotors, characterized by smaller-scale vortices that owe their origin to the breakdown of the boundary layer vortex sheet that is carried upward by the mountain wave. Yet none of the T-REX studies have documented the boundary layer separation (BLS) process itself. That is, in part, because of the design of the ground-based T-REX observing system that did not extend sufficiently high up on the Sierra Nevada steep lee slope. In addition, the environment in Owens Valley did not provide a sufficient number of scatterers in the boundary layer separation zone for the ground-based and airborne remote sensors.

Studies by Gohm and Mayr (2005) and Gohm et al. (2008) reported on observations from an airborne downward-pointing backscatter lidar. In both studies, the authors used measurements from the lidar along with associated numerical simulations to present evidence of boundary layer separation in the lee of the Dinaric Alps. However, the incoherent lidar did not provide any information on the flow structure within the BLS zone; thus, evaluation of the flow field depended on interpretation of the numerical simulation.

In this study, we focus on mountain waves and rotors documented in the lee of the Medicine Bow Mountains in southeastern Wyoming. The University of Wyoming King Air (UWKA) aircraft, carrying the Wyoming Cloud Radar (WCR), participated in a wintertime orographic precipitation experiment in 2006 [NASA Orographic Clouds Experiment 2006 (NASA06)]. During this experiment, the UWKA encountered two events of mountain-wave-induced turbulence. Direct penetrations of turbulent zones by aircraft carrying in situ instrumentation can be challenging and dangerous. However, combining in situ and remote sensing

instrumentation in a research aircraft offers the best potential for capturing and revealing the structures of rotor events with high spatial resolution (tens of meters) as well as the environmental parameters leading to their formation. Furthermore, the WCR was able to obtain the measurements all the way to the ground and thus document the lee-side BLS zone. As such, to the best of our knowledge, this study represents the first observational documentation of the wave-induced boundary layer separation.

The paper is organized as follows. In section 2, we describe the NASA06 field campaign, the measurements collected with the aircraft in situ probes and the cloud radar, and the dual-Doppler measurements and two-dimensional velocity field synthesis. In section 3, we introduce two BLS cases and describe the meteorological conditions. In sections 4 and 5, we present analysis and discussion of details from these two cases and summarize our results.

2. Field campaign and instrument measurements

a. NASA06

NASA06 was conducted in the mountainous region of southeastern Wyoming during January and February 2006. The focus of the project was to investigate the fine structure of deep wintertime orographic nimbostratus clouds and the processing of aerosols by these clouds. The UWKA, with a suite of in situ probes and the WCR, was used to collect data in clouds that formed over the Medicine Bow Mountains (MBM).

The MBM are a dome-shaped mountain range with a slight elongation along a 100-km-long axis that runs south-southeast–north-northwest from northern Colorado into southern Wyoming (Fig. 1). The highest peak, Medicine Bow Peak, is located in the northern half of the range, commonly referred to as the Snowy Range. It reaches 3650 m above mean sea level (MSL), about 1500 m above the surrounding plains. In its northern portion, the Snowy Range extends about 40 km across from west to east, and the northeastern flank is moderately steep with a slope of about 15%. The Sierra Madre Range (highest elevation is 3350 m MSL) lies 35 km to the west and south of the MBM. To the west and north, the high plains extend for over 200 km to the eastern flank of the Rocky Mountains, providing reasonably unobstructed upstream flow when the wind is from that direction.

During NASA06, the UWKA made seven flights focused on orographic clouds over the MBM and Snowy Range. On occasion, waves and rotors were observed in their lee. Here we report on data collected on 2 days,

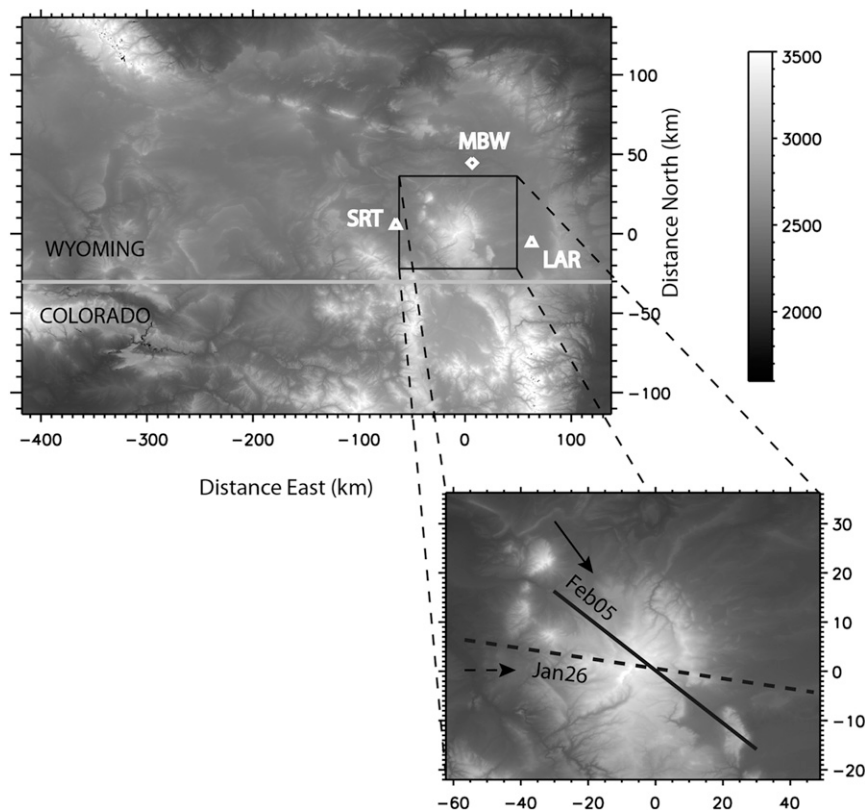


FIG. 1. Topography of the broader region through Wyoming and northern Colorado. The inset shows topography of the MBM and the region of interest for this study. Sample flight tracks for 26 Jan (dashed) and 5 Feb (solid) and the corresponding ridge-level wind directions are overlaid. The highest elevation in the MBM is 3650 m, and the surrounding plains are about 2100 m. The white triangles denote the locations of Laramie (LAR) and Saratoga (SRT). MBW denotes the location of the Medicine Bow Wind profiler. The plot is referenced to a ground research station near Medicine Bow Peak. Distance in the following figures is referenced from this ground station.

26 January and 5 February 2006, during which the UWKA made repeated passes aligned with the wind for an hour or longer, sampling the cap cloud and thermodynamics with in situ probes and profiling the reflectivity and velocity above and below the aircraft with the WCR (the instrument datasets used for this study are available upon request). Figure 1 shows a sample of the flight legs for the two events examined in this paper and the orography of the underlying mountains.

b. In situ measurements

The UWKA is a Beechcraft Super King Air 200T modified for research in the lower to midtroposphere (Rodi 2011). For NASA06, the UWKA was outfitted primarily for cloud physics measurements carrying instruments for measuring hydrometeors ranging from a few microns to several millimeters in diameter. For this study, these data are used to bound the limits of the estimated fall velocity of the scatterers, thereby providing an estimate of what

portion of the measured vertical Doppler velocity from the WCR is due to air motion alone (see the [appendix, section b](#)).

Wind and turbulence measurements are determined by combining measurements of dynamic and differential pressures from a five-hole gust probe on an extended nose boom and static pressure measurements from the aircraft static port near the rear of the aircraft with complementary filtered GPS and inertial reference system (IRS) measurements for aircraft position and attitude (Brown et al. 1983). The wind calculations rely on several calibration parameters that can be related to the geometry of the probe, the speed of the flow, and the relationship between probe position and the flow around the aircraft. These semiempirical parameters are determined by performing a set of maneuvers (Wendisch and Brenguier 2013) whereby the aircraft is flown in a way that encompasses nearly the full range of expected flow regimes during research flights. The best-fit

coefficients are determined by minimizing the variance of magnitude of the three-dimensional (3D) wind vector. The residual then provides some estimate of the expected uncertainty of the computed wind.

The systematic variation (tens of seconds and greater) in the error of the computed horizontal wind magnitude is about 1 m s^{-1} in straight and level flight. The drift of the vertical wind is smaller, about $\pm 0.5 \text{ m s}^{-1}$. Variation at shorter time scales (with the drift removed) is less by an order of magnitude. Spectra for the three components of the wind (not shown) suggest frequency response to at least 10 Hz in regions of weak to moderate turbulence. Thus, turbulent scales are resolvable to a few meters at typical research flight speeds of 85 m s^{-1} .

The atmospheric turbulence at the aircraft flight level is evaluated using the cubed root of the eddy dissipation rate [EDR $= \varepsilon^{1/3} (\text{m}^{2/3} \text{ s}^{-1})$; Sharman et al. 2014]. EDR has been adopted by the International Civil Aviation Organization (ICAO) as the standard metric for atmospheric turbulence reporting, in part because EDR is proportional to the RMS vertical acceleration an aircraft experiences, and it is the quantity to which aviation forecasts are made and validated. Here, EDR is estimated by two different methods: 1) by examining the power spectral density of the wind (horizontal or vertical) within a well-defined inertial subrange (Cornman et al. 1995) and 2) by the MacCready turbulence meter, which relates airspeed variation to EDR (MacCready 1964). For the first method, we utilize a frequency range that corresponds to spatial scales from 50 to 200 m. The total velocity variances in this frequency range are computed and related to the EDR for sliding 4-s data blocks (350 m). However, in regions of changing turbulence, the assumption of stationarity is not really valid. Regardless, results from both methods agree reasonably well (Feng 2001; Strauss et al. 2015). For the discussion presented here, EDR is taken from the MacCready meter.

A reverse-flow thermometer that utilizes a platinum-resistive wire element (Rodi and Spyers-Duran 1972) provides the primary temperature measurement. After correcting for dynamic effects, accuracy is better than $\pm 0.5^\circ\text{C}$. The second-order time response for the housing/wire system is no slower than 4 Hz, and it is thus sufficient to resolve variations at scales of a few tens of meters.

c. WCR measurements

The WCR is an airborne 95-GHz pulsed Doppler radar able to reveal fine details of cloud structure and dynamics. During NASA06, the radar utilized three fixed-pointing antennas with their beams aligned toward near-zenith, near-nadir, and approximately 30° forward of nadir. The WCR provides quasi-simultaneous vertical cross sections above and below the aircraft along the

flight track. The radar resolution volume at 1 km is about $10 \times 10 \times 30 \text{ m}^3$, and the typical sampling along the flight track and the radar radial range are 3 and 30 m, respectively.

All channels (antenna to receiver) were calibrated prior to the experiment, and the uncertainty was about $\pm 2 \text{ dB}$. During NASA06, scatterers were mostly ice particles. The minimum detectable signal of the least (most) sensitive down-forward (up) pointing radar beam was about -19 (-24) dBZ at 1 km.

The Doppler velocity measurements represent the along-beam component of the velocity of scatterers weighted by their reflectivity. The particles' mean velocity with respect to ground is retrieved from these measurements by correcting them for the aircraft velocity contribution into the beams (Damiani and Haimov 2006; Leon and Vali 1998). The overall accuracy of the aircraft motion correction is about 0.5 m s^{-1} . The maximum unambiguous velocity is $\pm 15.8 \text{ m s}^{-1}$. The aliased Doppler data segments were unfolded before any further analysis.

Single-Doppler data from the up- and down-pointing beams were used to estimate the scatterers' mean vertical velocity above and below the aircraft. The accuracy of the vertical particle motion estimates depends on the deviation of the beams from vertical and the strength of the horizontal winds. A correction for the horizontal wind contamination was applied by utilizing the aircraft-measured winds. Assuming no horizontal wind contamination, the vertical air motion is given by the difference between the mean motion and the mean terminal (fall) velocity of the particles.

d. WCR dual-Doppler measurements and synthesis

The Doppler measurements collected with the two down-pointing antennas provide data for a dual-Doppler (DD) synthesis of the two-dimensional (2D) scatterer velocity field in the vertical plane below the aircraft (Damiani and Haimov 2006; Leon et al. 2006). By decomposing the two radial velocity measurements, the projection of the 3D scatterers' motion on the plane determined by the beam directions may be resolved. Given the acquisition sampling rates and the radar resolution volume for the radar antennas used, the highest achievable 2D velocity field resolution is about $30 \times 30 \text{ m}^2$. For the DD processing in this study, we utilize grid resolutions from $30 \times 30 \text{ m}^2$ to $120 \times 100 \text{ m}^2$.

The DD synthesis leaves the third, cross-track component unresolved. This introduces an error in the estimate of the vertical wind component when the plane determined by the two down beams deviates from the vertical because of fluctuations in the aircraft roll angle. To minimize this error, an external estimate of the

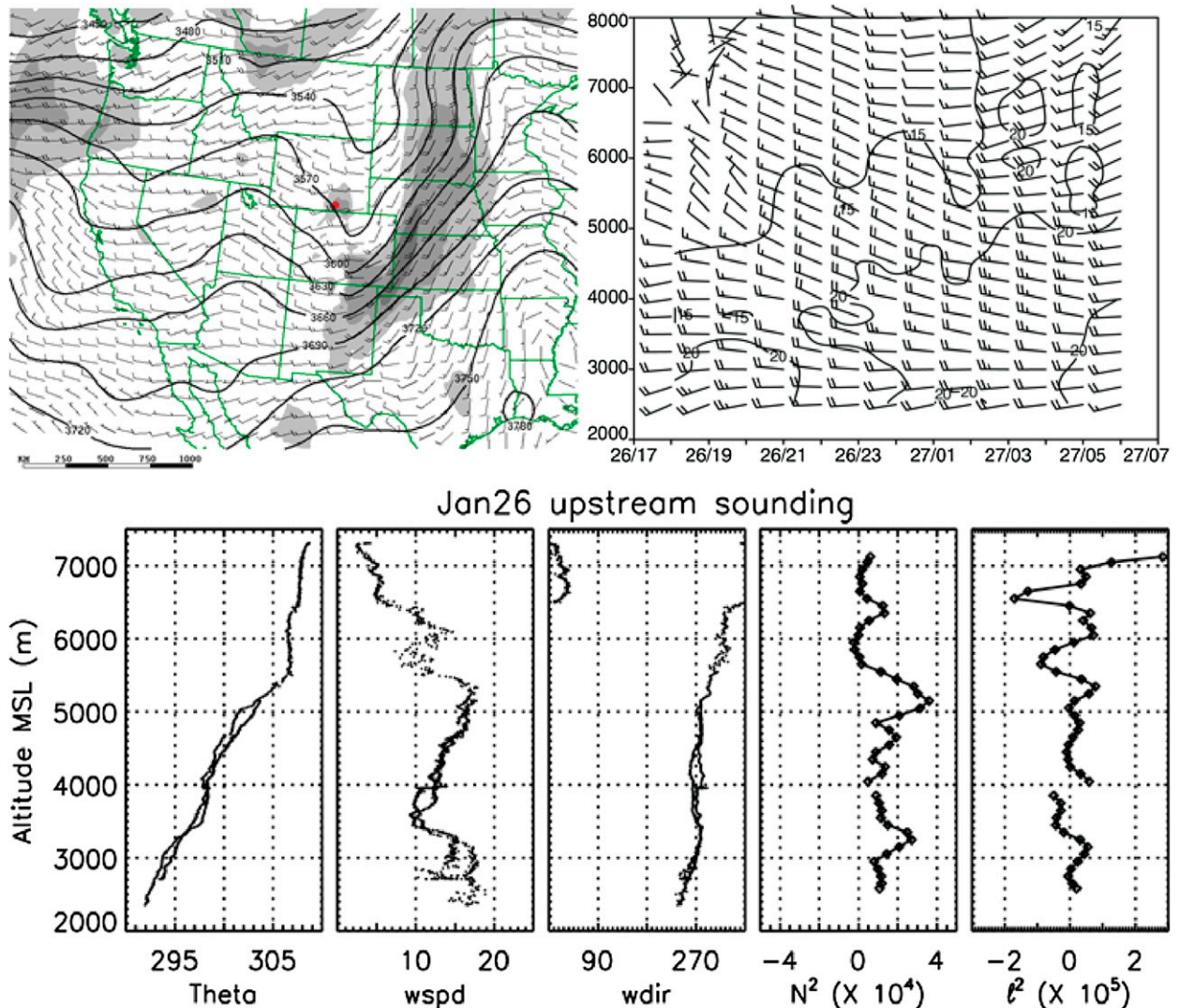


FIG. 2. (top left) Synoptic map showing 650-hPa heights, wind barbs, and isotachs for 1800 UTC 26 Jan; the red dot is MBM. (top right) Hourly wind profiles from 1800 UTC 26 Jan to 0600 UTC 27 Jan. Wind barbs and isotachs are in meters per second. (bottom) Potential temperature (K), wind speed (m s^{-1}), wind direction ($^{\circ}$), and squares of the Brunt–Väisälä frequency (s^{-2}) and the Scorer parameter (m^{-2}) from aircraft soundings at 1930 and 2020 UTC 26 Jan.

ambient wind using aircraft in situ measurements or sounding is utilized (Damiani and Haimov 2006).

The accuracy in the retrieved 2D air motion is affected by errors in the aircraft velocity, beam-pointing angles of the antennas, DD grid interpolation, and DD velocity retrieval; uncertainties as a result of the finite/low signal-to-noise ratio (SNR), finite radar resolution volume, and beam misalignment; uncertainties caused by the target temporal evolution and spatial advection between the two beams scans; and errors because of the unresolved crosswind component and the removal of the particles' fall velocity. A detailed analysis of the DD errors is given in Damiani and Haimov (2006). DD errors and

vertical air motion retrieval uncertainty associated with this study are discussed in the appendix.

3. Description of events and observations

a. 26 January 2006 event

Several hours prior to 1800 UTC 26 January, a strong synoptic-scale short wave passed through the observation area, as evidenced by the 650-hPa map of heights and wind over the western United States (Fig. 2, top left). Observations from a wind profiler located 55 km north of the Medicine Bow Peak (Fig. 2, top right) show

that, for the 12-h period beginning at 1800 UTC, winds from the surface to 4000 m MSL remained westerly with little variation in magnitude, about $15\text{--}20\text{ m s}^{-1}$, and little shear is present below 5000 m. However, prior to about 2000 UTC and between 4500 and 5500 m, there existed significant speed and directional shear: on the order of 0.05 s^{-1} .

Data from a slant aircraft sounding initiated at 1930 UTC and conducted from above and east of the highest peak to the west and north into the Saratoga Valley and a second minisounding from 2.7- to 5.2-km altitude conducted entirely within the Saratoga Valley about 50 min later are shown in the bottom panels of Fig. 2. Both reveal a stable layer of $3.5^\circ\text{C km}^{-1}$ between 2.4 and 5 km, with slightly stronger stratification at the mountaintop level. An inversion (12°C km^{-1}) is evident between 5.0 and 5.5 km, above which existed a near-neutral layer to the top of the sounding just over 7 km. This uppermost portion of the sounding from 5.5 to 7 km corresponds to the easternmost part of the flight track, over the mountain range. The portion below 5.5 km was flown west of the mountains. Maximum wind speeds are confined below approximately 3.2 km and weaken somewhat with time from 18 to 14 m s^{-1} an hour later. A sharp decrease in the winds occurred between 3.2 and 3.5 km with a minimum of about 9 m s^{-1} (wind shear of 10^{-2} s^{-1}). Above, to about 5.5 km, winds increased with height to 15 m s^{-1} . Wind direction was reasonably constant through the lowest layers, varying from about 250° to 280° . Profiles of the square of the Brunt–Väisälä frequency, $N = (g/\theta^* d\theta/dz)^{1/2}$, and the Scorer parameter, $l = [N^2/U^2 - (d^2U/dz^2)/U]^{1/2}$, are also shown. For both, the plotted values are averaged over 100 m to reduce noise. The value of N^2 is relatively constant throughout the lowest layers up to about 1000 m above the ridge crest, where it increases to about 3 times the lower-layer values, before decreasing again near the top of the sounding. The local nonlinearity parameter Nh/U is between about 1.3 and 1.5, where h is the crest height above the surrounding terrain, U (10 m s^{-1}) is wind speed at the crest, and N is 0.012 s^{-1} . These data suggest that, on 26 January, one may have expected some nonlinearity and possible wave breaking.

Between 2025 and 2210 UTC, the UWKA made five passes over the MBM. The first two passes were flown at 4300 m MSL, and the final three were flown at 5200 m MSL (hereafter, all flight altitudes refer to height above MSL). The first two legs were oriented more northwest–southeast and, hence, displaced farther south by about 5–10 km on the downwind side of the mountains. During the first two passes, the UWKA measured maximum horizontal winds of $25\text{--}27\text{ m s}^{-1}$ at 280° . In both passes, the maxima were located above the lee slope. Downstream

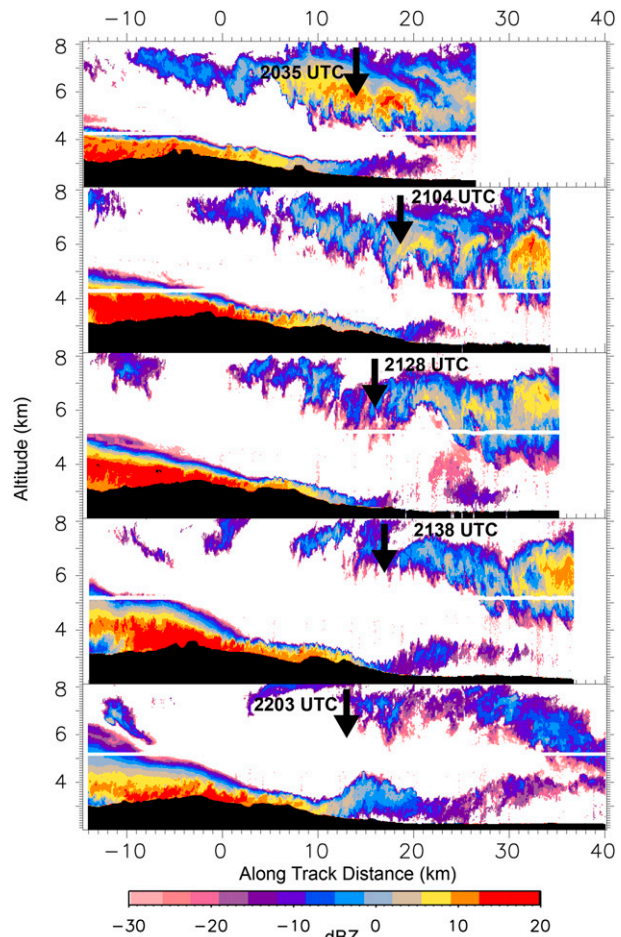


FIG. 3. Vertical cross sections of radar reflectivity from the up- and down-pointing beams for five cross-mountain legs on 26 Jan. There is 0.5–3.5-km cross-track displacement between legs. Black arrows with times point to approximate BLS occurrence. The orientation of legs is west-northwest–east-southeast. The wind direction is from left to right.

of the wind maxima, above the easternmost portion of the lee slope and the valley floor, the aircraft encountered a significant increase in turbulence with vertical wind variations of $\pm 5\text{ m s}^{-1}$.

Figure 3 shows vertical cross sections of reflectivity from the WCR for all five legs. Throughout the observation period, the orographic cloud top is significantly higher on the upwind side (compared to the downwind side) of the mountain. This tilting is due in part to the compression and acceleration of the flow over the lee slope. The slope of the cloud top increases with time and is on the order of about 100 m km^{-1} by leg 5. For all legs, the easternmost tail of the echo can be seen to separate from the surface (black arrows in Fig. 3), becoming more pronounced in the later legs. The location of this lifting of the echo corresponds to the maximum upward vertical velocity measured at flight level and, more generally,

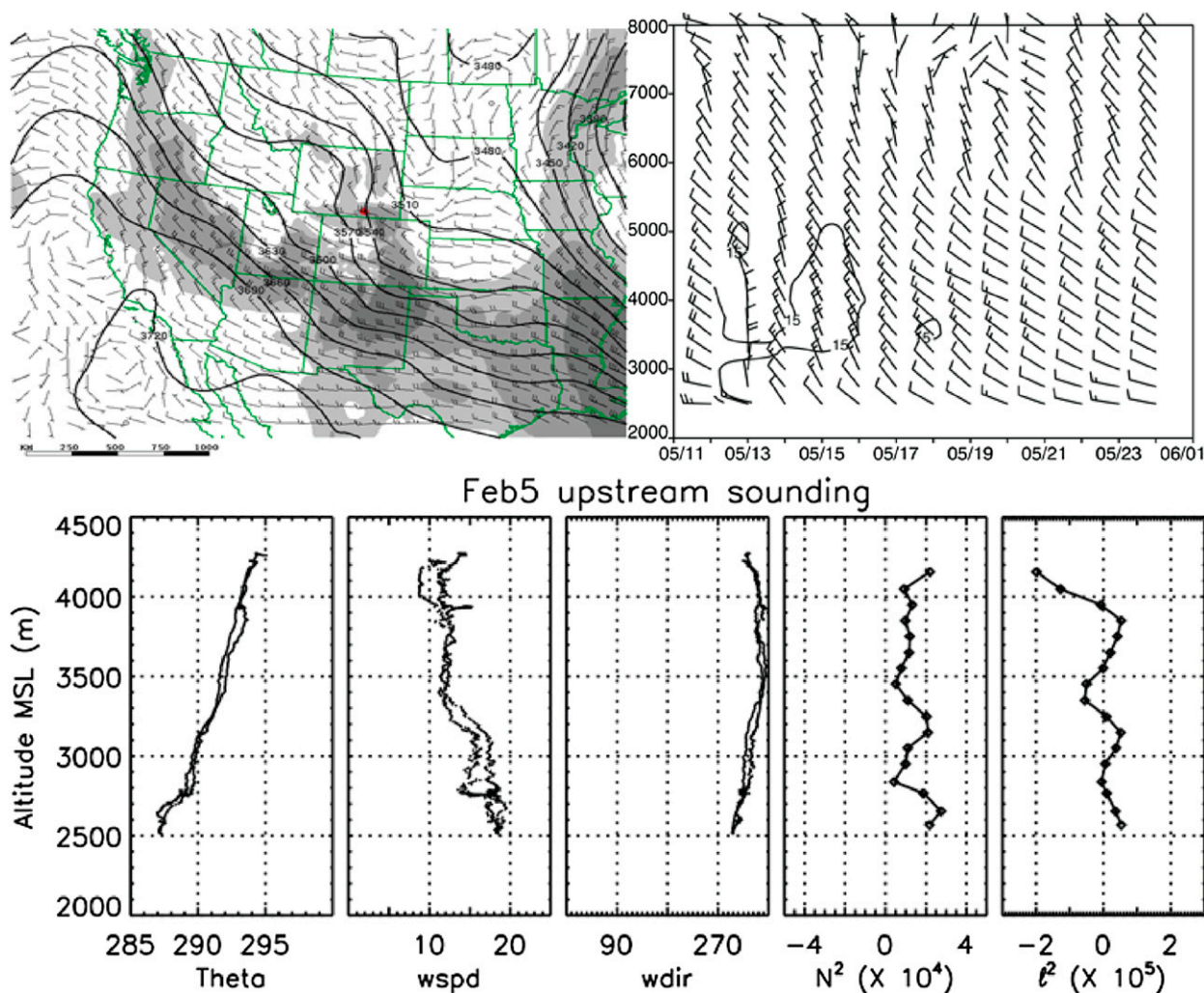


FIG. 4. As in Fig. 2, but for 5 Feb. (top left) The synoptic chart is from 1200 UTC, and (bottom) the aircraft sounding is from 1430 UTC; (top right) hourly wind profiles are from 1200 UTC 5 Feb to 0000 UTC 6 Feb.

to the location of transition from smooth to turbulent flow, as measured at the aircraft flight level. Also note that, between legs 3 and 5, the location of the lift feature propagates upstream by as much as 7 km in 30 min (deviations in locations from earlier legs may be a result in differences in downwind location of the aircraft track). Taken together, the observations from all five passes paint a picture of an event that gained strength in the midlevels as observed by the UWKA over the first hour of observations and then, over the last half hour, transitioned into a much stronger surface event, featuring a downslope windstorm, wave-induced boundary layer separation, and a low-level rotor.

b. 5 February 2006 event

The synoptic conditions at 1200 UTC 5 February were characterized by a weak short wave rapidly approaching

the study area from the northwest, embedded on the backside of a broad trough located several hundred kilometers to the east (Fig. 4). The 650-hPa-level winds were west-northwesterly at about 15 ms^{-1} . The approaching short wave provided some slight instability at midlevels, leading to significant cloud cover and light to moderate orographically enhanced snow over the mountains, as well as a shift to more northwesterly winds with a corresponding decrease in the wind speed. Hourly wind profiles show winds of $15\text{--}20 \text{ ms}^{-1}$ out of the northwest, decreasing somewhat and becoming northerly at 1300 UTC before backing to the northwest following the passage of the short wave. A 60–90-min difference between the profiler-measured winds and the winds at Medicine Bow Peak are expected, assuming the short wave is propagating at or about half of the mean wind speed.

An aircraft sounding, taken in the Saratoga Valley between 1425 and 1440 UTC, shows that the winds at 650 hPa had already shifted back to the northwest but remained at 15 m s^{-1} . A wind speed maximum (19 m s^{-1}) occurred near the surface and was more westerly. Thermodynamic data from the sounding reveal a moist stable layer below the mountaintop level. The value of N^2 is relatively constant throughout the depth of the sounding. Near the top of the sounding, about 1000 m above ridge crest, \bar{l}^2 decreases sharply with altitude and becomes negative. Based on linear theory, a sharp decrease of the Scorer parameter with height represents conditions conducive to trapping of wave energy and formation of lee waves (Nappo 2002). Further analysis shows that, throughout most of the depth of the sounding, \bar{l}^2 is slightly greater than k^2 , where k is the horizontal wavenumber estimated from the aircraft data to be $8.3 \times 10^{-5} \text{ m}^{-1}$. Based on linear theory, again, this would indicate a medium supportive of vertically propagating gravity waves. At the top of the sounding, \bar{l}^2 becomes significantly less than k^2 , favoring a partial reflection of wave energy below that level and potentially the onset of lee waves. This sharp decrease of the Scorer parameter with height is apparently caused by the wind profile curvature term, which is rather large at this height because of a minimum in the wind speed profile. The local nonlinearity parameter Nh/U is about 0.85 at ridge-crest level. Taken together, one may expect the formation of trapped lee waves, although the evidence suggesting that is not overwhelming.

Between 1400 and 1500 UTC, the King Air made four passes over the MBM and the Snowy Range. The first pass was made at 5200 m and the next three at 4200 m, oriented along the mean wind direction at flight level. For all the legs, the flight-level wind direction upstream of the Snowy Range is between 320° and 330° , with speeds of about 15 m s^{-1} (except for the first leg, which had slightly higher speeds but was also flown 1000 m higher in altitude).

Figure 5 shows cross sections of WCR-measured vertical velocity for each leg; times are indicated on the figure. The thick black vertical lines indicate the locations of the primary wave crest based on the WCR measurements. The location of the wave crest from the WCR data agrees with the flight-level vertical wind and thermodynamic data from the King Air. Both the flight-level data and measurements from the WCR show an upstream migration of the primary wave crest from the first to the third leg, with the wave-crest location remaining stationary following leg 3. Furthermore, both the WCR data and the flight-level data suggest that, during the first leg at 1400 UTC, a clear primary wave with a moderate degree of turbulence downstream

(possibly collocated in a weak secondary wave) exists. In leg 3, 47 min later, this transitions to a well-defined lee wave train with at least two wave crests and little turbulence.

4. Event analyses and discussion

The following analysis and discussion is not presented in a chronological order for the events, but rather in a way that best highlights the similarities and differences between the two events. Here, we focus on three major aspects of the observations.

a. Wave-rotor structure

The general structure of the wave-rotor system on 5 February is well represented by the data from two legs shown in Fig. 6. The left panels show horizontal and vertical winds, potential temperature, and EDR from the aircraft (top) and the two-dimensional wind vectors overlaid on the horizontal wind speed for the retrieved DD velocity field (bottom) from leg 1. At the level of the aircraft directly above the highest terrain, the potential temperature rapidly increases by 3 K, and continues to increase by another 2 K about 7 km downstream over the lee slope. This is also the area of maximum observed downdraft, 4 m s^{-1} , from the aircraft and increasing horizontal winds near the surface because of accelerating downslope flow (Fig. 6, bottom left). At the aircraft flight level, there is a moderate decrease in the horizontal wind, from 21 to 9 m s^{-1} corresponding to the area of maximum perturbation of the potential temperature. The trace of the vertical velocity through this region lacks a classical smooth wave structure; rather, it is suggestive of some turbulence (to be investigated in the next section).

At about one-third of the distance down the slope, the aircraft-measured vertical velocity becomes positive (upward motion) and passes through peaks of about 4 m s^{-1} . This portion of the lee wave, upwind of the primary crest, corresponds to the region directly beneath it where (i) the strong-wind layer near the surface uplifts and (ii) the boundary layer above the mountain lee side separates, as evidenced from the DD analyses. Figure 7 (leg 1, top) shows the vorticity field from the same analyses. The spanwise vorticity in the low-level jet plunging down the slope is mostly determined by the vertical shear. Hence, positive (negative) vorticity is found below (above) the jet. The very near-surface positive vorticity sheet is lifted about 700 m above the ground between about $x = 7$ and 12 km. This location corresponds to the upwind edge of the wave and is easier to visualize from the lifting of the negative vorticity sheet that caps the downslope flow at a height between

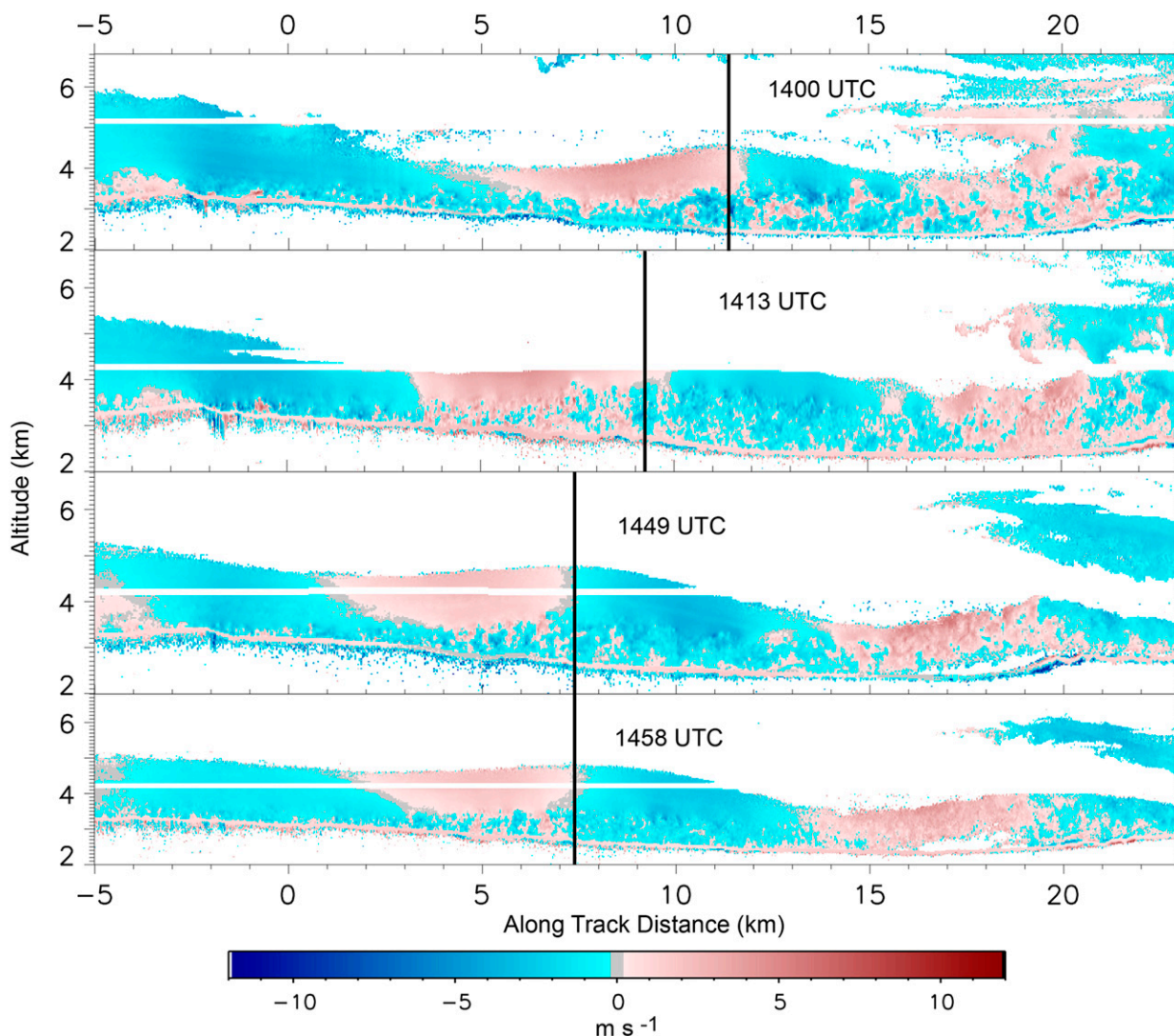


FIG. 5. Cross section of vertical Doppler velocity from the up- and down-pointing beams for four legs from 5 Feb. Warm colors are positive and indicate upward-moving air. Orientation is from northwest to southeast, and the wind is from left to right. The solid white line at (top) 5.2 and (top middle)–(bottom) 4.2 km represents the flight level of the aircraft with the resulting roughly 200-m-deep blind zone near the aircraft. The underlying terrain varies in altitude from about 3.5 km on the left side (highest terrain) to 2.25 km on the right side (Laramie Valley).

3.5 and 4 km. Underneath this crest, a weak return flow (Fig. 6, bottom left) of $2\text{--}4\text{ m s}^{-1}$ exists. The return flow in the rotor extends up to about 300–500 m above the surface. Based on the one wave crest discernable in the DD analysis, we estimate the horizontal wavelength of the wave aloft to be about 10–15 km. However, neither the radar data nor the measurements from the aircraft suggest any further wave activity downstream. Calculated streamlines (not shown) indicate rather smooth flow down the lee slope and into the leading edge of the rotor. Once the flow passes through the crest and begins to decelerate, small eddies (subrotors; Doyle et al. 2009;

Doyle and Durran 2007) begin to appear along the high-shear interface that separates the main flow and the return flow in the rotor.

The character of the system changes significantly 45 min later, as documented along leg 3 (Fig. 6, right). Aircraft measurements from leg 3 reveal smooth flow with a classic wave train beginning above the peak and extending at least 25 km downwind to the end of the leg. Although leg 3 was flown 1000 m lower than leg 1, both the single-Doppler velocities (Fig. 5) and the DD synthesis (Fig. 6, bottom-right) support this assertion. The in situ aircraft data show a strong correlation between

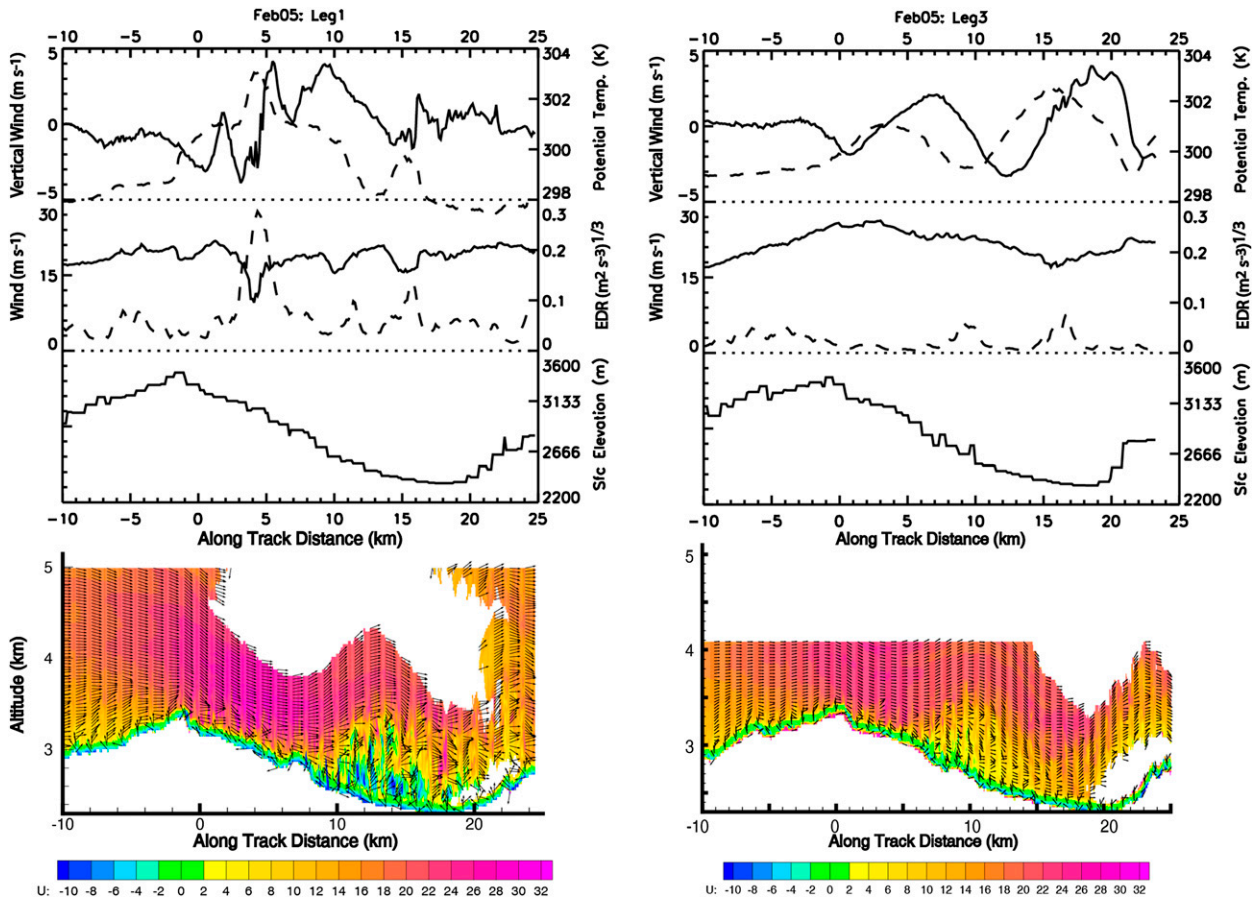


FIG. 6. Data from (left) leg 1 (5.2 km MSL) and (right) leg 3 (4.2 km MSL) on 5 Feb. The line plots are of flight-level data and show (top) vertical velocity (solid) and potential temperature (dashed), (middle) horizontal wind speed (solid) and EDR (dashed), and (bottom) the underlying topography. (bottom) Results of the DD analysis with wind vectors showing the wind direction only (not scaled for the wind magnitude) overlaid on a color field for the retrieved along-plane component of the horizontal wind. A high-resolution version of this figure is available in the online supplement.

potential temperature and vertical velocity variations with a phase shift of 90° . The horizontal wind, however, shows no correlation with either vertical wind or potential temperature, although the variation of the horizontal wind is quite large, from 15 m s^{-1} upwind of the peak to nearly 30 m s^{-1} just downwind of the highest terrain. This, coupled with the radar analysis, suggests that the aircraft sampled within the descending branch of the mountain wave above the accelerating downslope flow on the lee side. The maximum downslope wind is weakened somewhat, from 32 m s^{-1} in leg 1 to about 25 m s^{-1} by leg 3. The lifting of this layer near the bottom of the slope has propagated a few kilometers upstream (see Fig. 5), and the maximum vertical displacement is less, about 300 m. Flow near the surface beneath the wave is weak, but unlike in leg 1, no evidence of return flow exists. The DD analysis shown in Fig. 6, and streamline calculations (not shown) suggest much

smoother flow downstream of the first lee-wave crest and through the second crest, consistent with the aircraft measurements.

The vertical motion, potential temperature variations, and variation in horizontal wind measured at the aircraft flight level during legs 3 and 5 on 26 January are shown in Fig. 8. The two legs were separated in time by 40 min, and the observations suggest significant dynamical evolution of the flow during this time. Furthermore, the perturbations on 26 January were much larger than on 5 February. Along leg 3, the potential temperature increases from 304 K on the upstream side of the mountain to a maximum of 308 K just a few kilometers downwind of the highest terrain. Throughout the upwind portion of this leg, the vertical velocity is close to zero, the horizontal wind remains constant (about 18 m s^{-2}), and there is little or no turbulence. The vertical velocity shows no coherent structure, but the horizontal wind

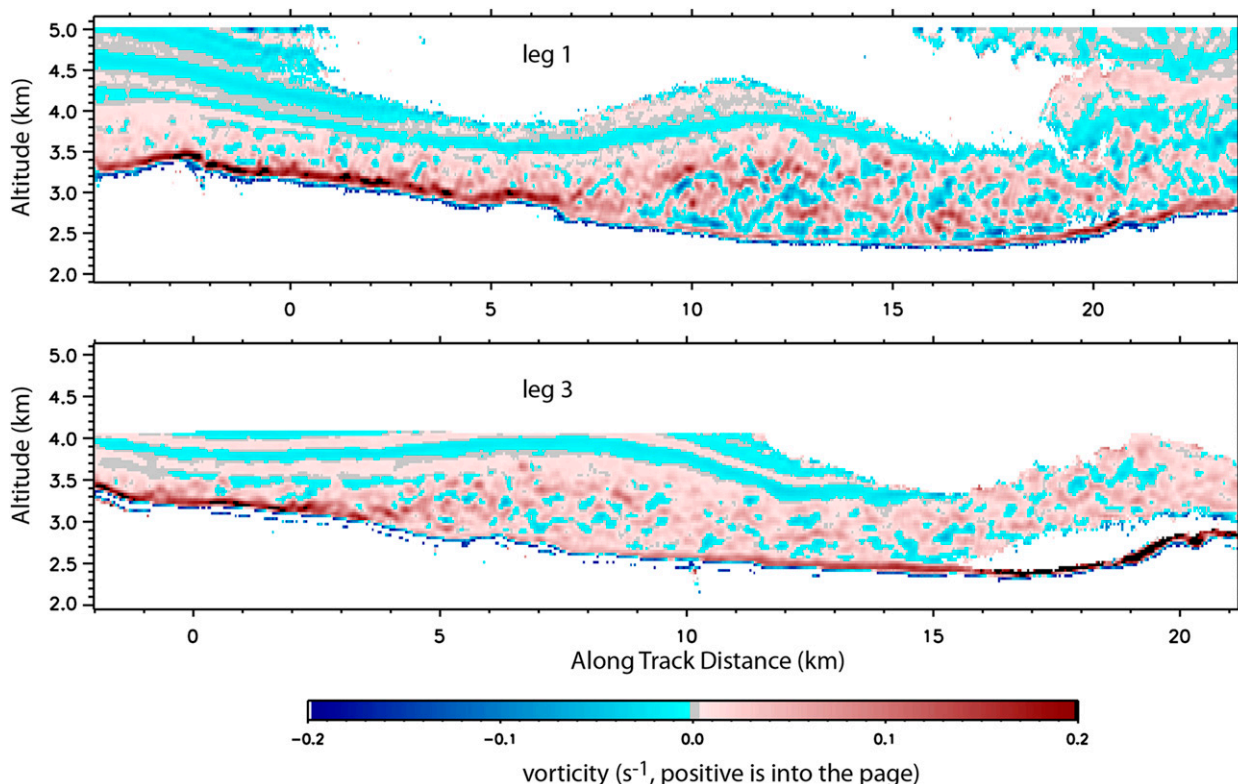


FIG. 7. Calculated cross-track horizontal component of vorticity for (top) leg 1 and (bottom) leg 3 on 5 Feb. Warm colors indicate positive vorticity, pointing into the page.

speed decreases to near zero by 12 km downstream of the highest terrain and remains near zero over the next 8–10 km just to the beginning of the valley. Near the ground, where one may expect a strong near-surface downslope flow, no DD analysis is available because of the lack of signal caused by insufficient scatterers. Further downwind and over the foot of the lee slope, the aircraft flight level in situ measurements show a very rapid drop in potential temperature (>4 K over a few hundred meters), corresponding to a sharp-edged updraft of 12 m s^{-1} that is approximately 1 km wide. The updraft is followed by a somewhat broader, more diffuse and turbulent downdraft of 7 m s^{-1} . Just upwind of the sharp updraft, the horizontal wind speed increases from near 0 to approximately 15 m s^{-1} . This updraft–downdraft couplet corresponds to the zone within the reflectivity image (Fig. 3, third panel) that shows a “dome” above the aircraft flight level where scatterers are first carried to higher altitudes (in the updraft) and then brought back down to lower altitudes (in the downdraft). Such a strong gradient in potential temperature and sharp-edge boundary of the updraft, along with the nearly stagnant flow immediately upstream, is suggestive of gravity wave breaking (Lilly 1978).

Observations during leg 4 (not shown) reveal similar characteristics to those obtained just 10 min prior during leg 3. There remains a sharp decrease (~ 4 K) in the potential temperature; however, it is not as abrupt as in the previous leg, and the corresponding updraft region is broader and less turbulent. The horizontal wind decreases to near zero for a few kilometers on the upwind side of the maximum updraft.

At 25 min after leg 4 and nearly 40 min after leg 3, the variations measured at the aircraft flight level continue to lessen (Fig. 8, right) but are still considerably larger than anything encountered on 5 February. Also, by this time, the scatterers advect far enough downstream and into the valley to provide sufficient radar echo and allow DD analysis, revealing more characteristics within the flow field beneath the aircraft. The potential temperature at flight level increases from 302 K well upstream of the barrier to 308 K above a point roughly halfway down the lee slope. Just downwind of the highest terrain, there is a weak (1 m s^{-1}) downdraft about 8 km wide. Throughout the downdraft and farther downstream, the horizontal wind decreases to about 8 m s^{-1} , half of its upstream value. The updraft–downdraft couplet is discernible in the aircraft in situ

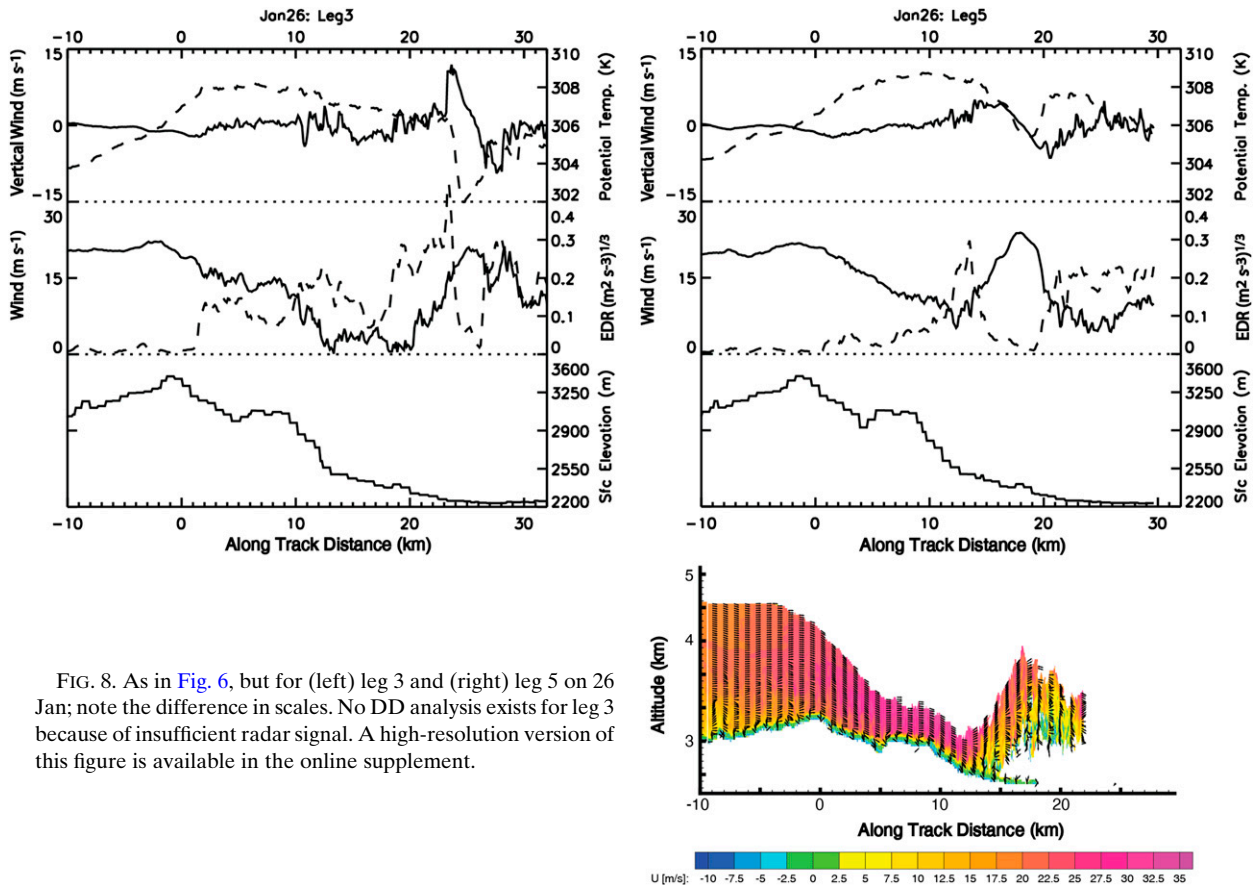


FIG. 8. As in Fig. 6, but for (left) leg 3 and (right) leg 5 on 26 Jan; note the difference in scales. No DD analysis exists for leg 3 because of insufficient radar signal. A high-resolution version of this figure is available in the online supplement.

data, but the magnitude is less ($\pm 5 \text{ m s}^{-1}$), and the corresponding potential temperature anomaly (2 K) is weaker than in both previous legs. Between legs 3/4 and leg 5, the couplet propagates upstream about 7 km. The DD analysis shows strong downslope flow of 35 m s^{-1} just a few hundred meters above the ground. Near the valley, this layer of strong winds separates from the surface and is lifted 1 km above the valley floor. The analysis suggests some return flow beneath the elevated layer of strong winds, although it is difficult to quantify because of the weakened signal as the majority of the scatterers become lofted.

While the boundary layer separation seems to be present and well documented by our measurements in both the 26 January and 5 February cases, there are some key differences between these two events. The 5 February case has an appearance of a classic lee-wave rotor (Doyle and Durran 2002). This is supported by the phase relationship between the potential temperature and vertical velocity at the flight level and the attendant weaker and somewhat turbulent flow located underneath the wave crest

that is topped by the separated layer of stronger winds aloft.

In the 26 January case, there is little evidence of a coherent wave structure at the flight level; rather, the aircraft in situ measurements are strongly suggestive of the gravity wave breaking at the flight level during the time of leg 3 and perhaps leg 4, but ceasing by leg 5. The near-surface flow over the lee slope, as inferred from the DD analysis, is much stronger than the wind speeds encountered at the aircraft flight level. In particular, overlying the strongly accelerated flow down the lee slope is a region of stagnant flow aloft. The wave perturbation causing the boundary layer separation appears below the flight level, closer to the valley floor. The updrafts both at flight level and upwind of the boundary layer separation zone near the ground are rather sharp. The flow features documented in the 26 January event are more suggestive of an atmospheric analog to a hydraulic jump than a lee-wave rotor (Vosper 2004; Hertenstein and Kuettner 2005; Hertenstein 2009; Armi and Mayr 2011). However, unlike in these previous studies, which show a strong

inversion at near-mountaintop level, no such inversion was present on 26 January. From that standpoint, this case is more similar to one modeled by [Jiang et al. \(2007\)](#). [Jiang et al. \(2007\)](#) investigate nonlinear effects on boundary layer separation in an atmosphere with constant N^2 and uniform wind speed. As the non-dimensional ridge height increases, the steepness of the induced mountain waves also increase, eventually leading to wave breaking in the midtroposphere. Below the wave primary crest, a downslope windstorm develops, and, farther downstream, in response to the strong updraft, BLS separation occurs and a rotor develops. The specific dynamics of the 26 January case is further investigated in [Grubišić et al. \(2015, hereafter Part II\)](#).

b. Turbulence characteristics

Turbulence characteristics for both events can be investigated by direct measures of horizontal and vertical wind speed at the aircraft flight level as well as inferred turbulence based on DD analyses below the aircraft in regions where sufficient echo exists. A detailed analysis of the turbulent properties derived from the radar analysis is presented by [Strauss et al. \(2015\)](#); here, we focus on a description based primarily on the aircraft in situ measurements.

During 26 January, the UWKA encountered significant turbulence on the upwind and downwind side of the updraft–downdraft couplet ([Fig. 8](#), top left). Well upwind of the couplet, over the lee slope, EDR from the MacCready turbulence meter ranges from 0.1 to $0.2 \text{ m}^{2/3} \text{ s}^{-1}$ through the roughly 10-km region during leg 3, with values of $0.05\text{--}0.12 \text{ m}^{2/3} \text{ s}^{-1}$ (light turbulence) over a slightly shorter region during leg 5. Just on the upwind side of the couplet, EDR increases to more than $0.4 \text{ m}^{2/3} \text{ s}^{-1}$ in leg 3 and $0.3 \text{ m}^{2/3} \text{ s}^{-1}$ during leg 5 (moderate to strong turbulence). For both legs, the main updraft and transition to downdraft are nearly devoid of turbulence (EDRs less than $0.05 \text{ m}^{2/3} \text{ s}^{-1}$) before again increasing downwind of the couplet, with EDRs of 0.3 and $0.2 \text{ m}^{2/3} \text{ s}^{-1}$ during legs 3 and 5, respectively.

On both sides of the couplet, the turbulence is larger during the earlier leg than for the later one. Note that the earlier leg also has significantly larger variations in the vertical velocity and potential temperature. Power spectra computed from these data (not shown) do not reveal any dominant scales for the turbulence. However, it is clear that there are no coherent structures at frequencies higher than 1 Hz (spatial scales less than 100 m).

On 5 February, the turbulence encountered at the level of the aircraft is significantly less ([Fig. 6](#), top). During leg 1, there appears some brief moderate

turbulence with EDR up to about $0.25 \text{ m}^{2/3} \text{ s}^{-1}$ on the upwind side of strongest updraft. Upstream of this, EDR values are less than $0.05 \text{ m}^{2/3} \text{ s}^{-1}$, and downstream EDR values are between 0.05 and $0.1 \text{ m}^{2/3} \text{ s}^{-1}$. Along leg 3, all EDR values at the aircraft level are less than $0.06 \text{ m}^{2/3} \text{ s}^{-1}$. Below the aircraft, during the earlier legs, data from the radar suggest some turbulence being generated in the location of the rotor and likely being advected downstream, potentially as shedded vortices ([Fig. 5](#), top, and [Fig. 6](#), bottom left). The vertical Doppler velocity field reveals significant speckling underneath the crest of the wave, extending downstream and increasing in vertical extent. This feature is observed strongest during legs 1 and 2 and becomes significantly reduced during the later legs, corresponding to the time with little or no reverse flow beneath the wave crest.

c. Observations of subrotors

During the 26 January event, snow and ice scatterers are carried down the lee slope in the strong near-surface flow before being lofted nearly 1 km as the flow separates from the surface. [Figure 9](#) shows results from the DD streamline analysis from leg 5 on 26 January, enlarged to allow viewing fine details of the flow field. The streamlines are overlaid on the retrieved vertical velocity field. On the front side of the wave, the streamlines suggest smooth flow. However, beneath and within the interior of the rotor, behind the zone of boundary layer separation, the streamlines rotate back around themselves in several locations. These eddies are likely produced by the shear along the interface between the strong flow in the wave and the much weaker flow beneath it. Although the streamlines are an instantaneous snapshot of the flow field, one envisions eddies, or subrotors, that are confined to very near the surface and beneath the wave on the uplift portion of the wave to advect with the flow and through the wave farther downstream.

These subrotors can also be investigated by computing the cross-track component of the horizontal vorticity ([Fig. 10](#)). The top panel shows the vorticity calculated on a $30 \times 30 \text{ m}^2$ DD grid. The resultant field is smoothed using a $150 \times 90 \text{ m}^2$ filter to reduce the noise. Several strong positive anomalies can be seen between 15 and 18 km within the same region as in the streamline analysis. While the larger-scale flow is relatively stationary, at least at time scales for the DD analysis, advecting subrotors are likely not. Thus, to test the coherency of these features, we also computed a vorticity field based on a larger ($120 \times 100 \text{ m}^2$) DD grid ([Fig. 10](#), bottom). At this grid resolution, any feature that shows up should not be strongly influenced by errors associated with advection through the flow field. Indeed, several relatively

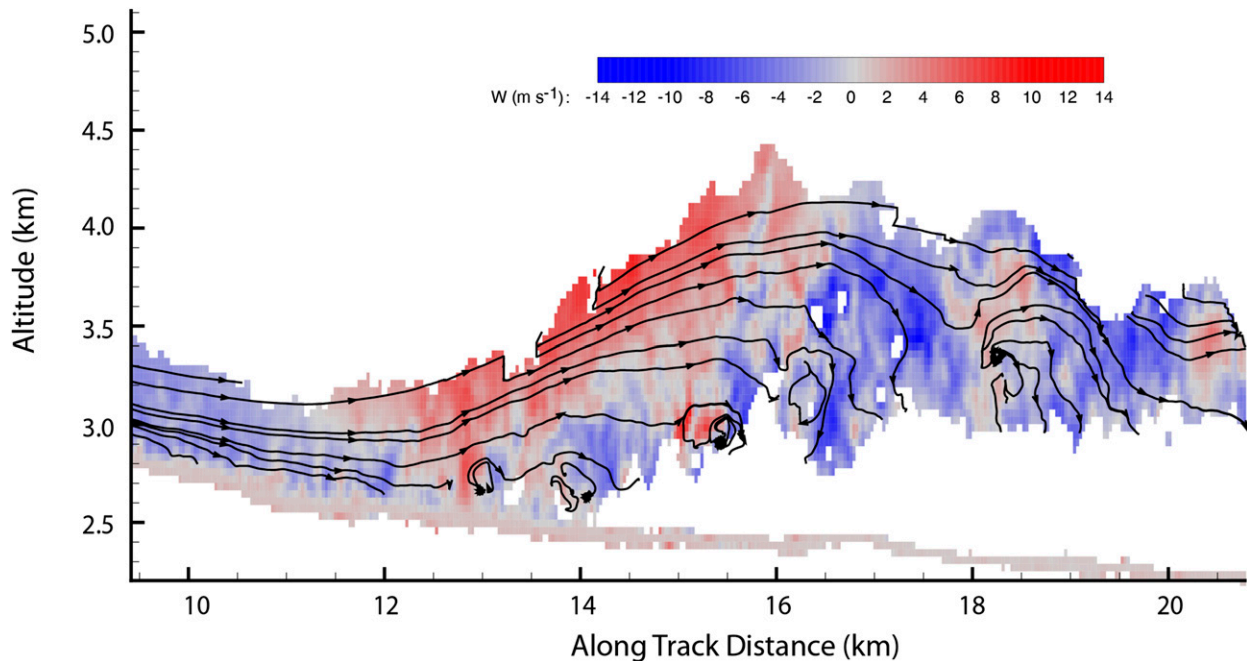


FIG. 9. DD analysis from leg 5 on 26 Jan. The image shows an enlarged region of the near-surface rotor. The streamlines are overlaid on the retrieved vertical air velocity; warm colors indicate positive (upward) motion.

strong positive vorticity anomalies remain in the center of the wave. These features have roughly equal horizontal and vertical extent from 500 m to about 1 km.

The existence of subrotors has long been postulated based on modeling (Doyle and Durran 2002, 2007; Doyle et al. 2009) and, indeed, time-lapse video of clouds has captured subrotor-type eddies (Ozawa et al. 1998). More recently, the array of ground-based instrumentation in T-REX allowed the first direct observation of subrotors (Hill et al. 2010) from lidars and inferred occurrences from ground-based wind profilers (Cohn et al. 2011). The observations presented here show subrotors existing within a larger rotor structure, at least qualitatively in agreement with earlier modeling and observational studies.

5. Summary and conclusions

In this study, we presented the analysis of observations from two wave-induced boundary layer separation (BLS) events that occurred in the lee of the Medicine Bow Mountains (MBM) in southeastern Wyoming. The key observations for both of these events come from multiple aircraft legs over a period of an hour or more flown over the MBM by the University of Wyoming King Air. The airborne in situ measurements provide some context for the dynamic and thermodynamic structure of the atmosphere over the mountain and

above the BLS events. Further, detailed observations from a millimeter-wavelength radar provide unprecedented measures of the 2D dynamic field within the rotors and represent the first airborne radar observations of a boundary layer separation and atmospheric rotors. We also document the intermittency and strength of turbulence in these two rotor events.

The observational evidence supports the conjecture that the evolution and forcing of the two events was quite different. Reverse flow in the BLS event on 5 February is only observed during the first leg; there is no evidence of reverse flow beneath the wave crests in subsequent legs. The lack of strong thermodynamic or dynamic signals at the aircraft flight level (small vertical velocities, weak turbulence), suggest that this event is primarily a boundary layer phenomenon bearing resemblance to a lee-wave (Type I) rotor (Hertenstein and Kuettner 2005). The DD analysis shows evidence of turbulent structures being present already at the leading edge of a single rotor. No secondary wave crests and/or rotors underneath are visible downstream. Later in the observation period, the single wave crest/rotor transitions into a train of trapped lee waves, as evidenced both in the radar and in the aircraft data.

The 26 January event is much more dynamic: more intense and unsteady. In situ observations at the aircraft flight level reveal vertical velocities in excess of $\pm 12 \text{ m s}^{-1}$ and moderate to strong turbulence 1700 m

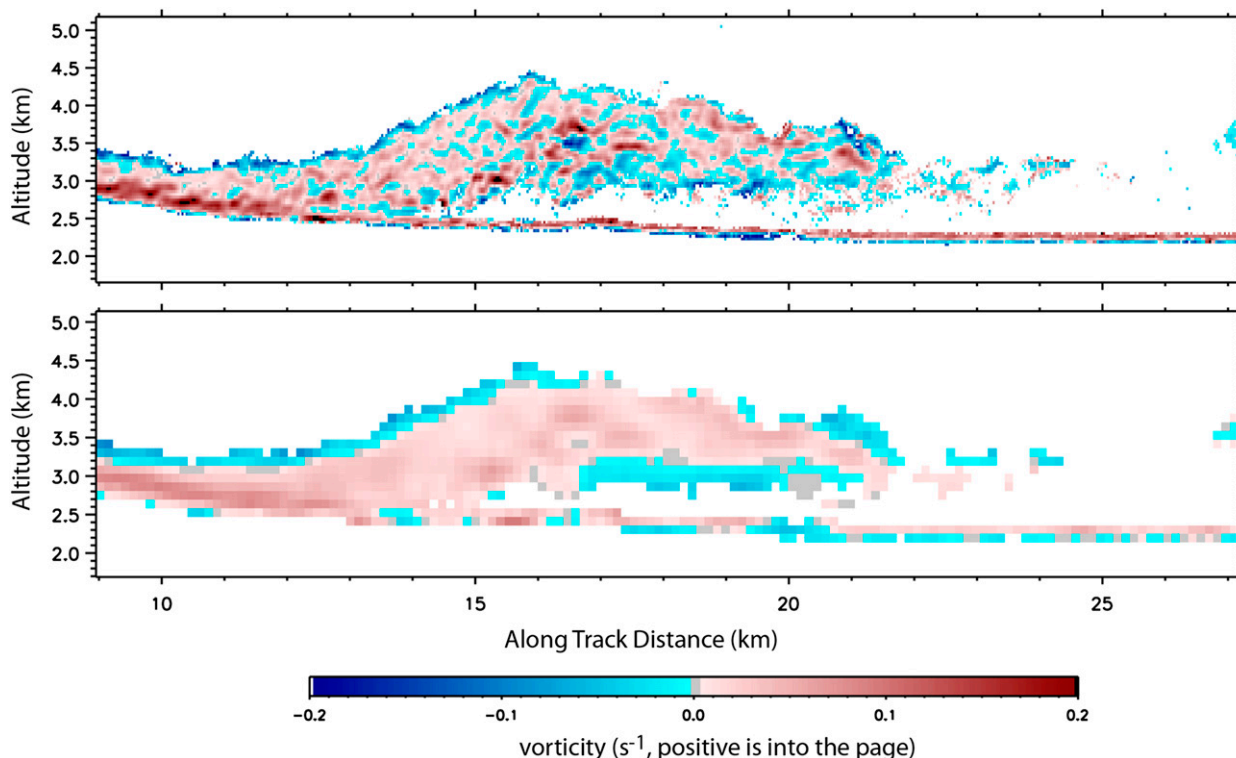


FIG. 10. Calculated cross-track horizontal component of vorticity for leg 5 on 26 Jan. Sign convention is as in Fig. 7. (top) Vorticity calculated based on a DD analysis conducted on a $30 \times 30 \text{ m}^2$ grid; the resultant field is smoothed by a $150 \times 90 \text{ m}^2$ moving-average filter to reduce the noise. (bottom) Vorticity based on a DD grid of $120 \times 100 \text{ m}^2$ (to test for coherency; see text) and then smoothed.

above the highest terrain on multiple legs. In situ kinematic and thermodynamic measurements suggest wave breaking occurring above the lee slope at and above the flight level. The sharp dome in the WCR reflectivity echo above the level of the King Air during the third penetration suggests some depth to the strong upward vertical motion measured by the aircraft at flight level. The separation of the echo at the ground throughout the entire 90-min observation period further suggests this phenomenon extends down to the surface. DD analysis shows very strong near-surface flow over the lee slope that separates abruptly from the ground with strong upward vertical motion. All of this paints a picture of an event that more resembles an atmospheric internal hydraulic jump than a lee-wave rotor.

Our observations of the rotor and its internal structure consisting of smaller-scale vortices, or subrotors, are in qualitative agreement with the findings from earlier modeling (Doyle and Durran 2007; Doyle et al. 2009) and observational studies (Hill et al. 2010). However, unlike Hill et al. (2010), we did not observe any subrotors outside of the main rotor structure. The spatial scale of the subrotors appears to be on the order of 500 m–1 km, whereas the scale of the larger (main) rotor

is about an order of magnitude larger (5–10 km). The nature of the observations makes it difficult to say much about the temporal coherency aside from the fact that the event on 26 January persisted for more than 90 min and that we observed a significant flow transition during the 5 February event.

Last, herein we demonstrated the utility of an airborne cloud radar to investigate the dynamics of atmospheric rotors. Because of their proximity to the ground in complex terrain and association with moderate or even severe turbulence, few direct observations of rotors exist. We have shown that, under the right conditions with sufficient scatterers (i.e., presence of falling and blowing snow/ice), rotors can be thoroughly observed using airborne remote sensing techniques.

In Part II, we investigate further the events described herein with the aid of a mesoscale numerical weather prediction model. Analyses focus on the dynamics and the evolution of the boundary layer separation events and the ability of the model to capture the character of the observations.

Acknowledgments. This work was supported in part through NSF collaborative Grants ATM-0742110 and

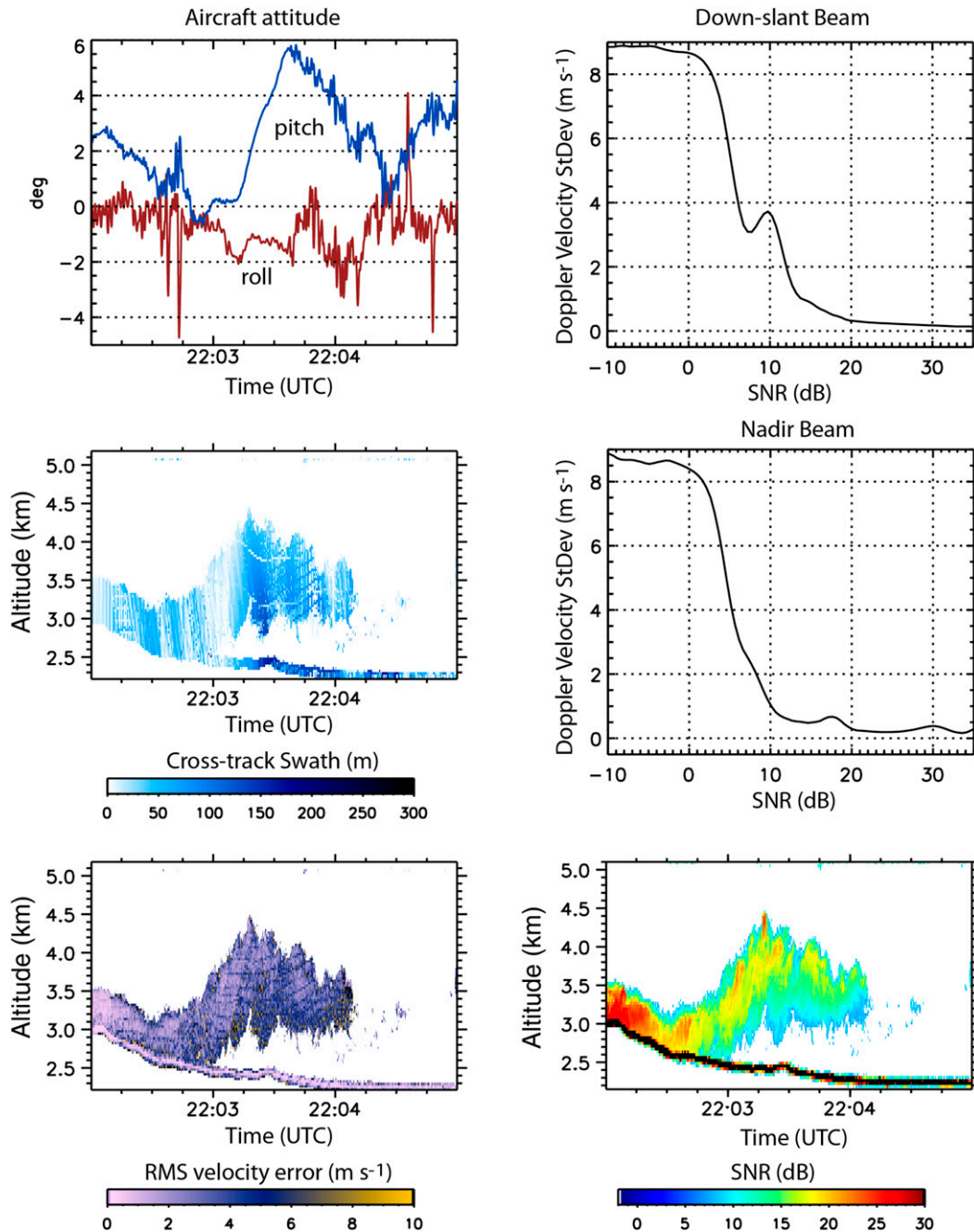


FIG. A1. Illustration of DD error analysis for leg 5 during the 26 Jan case. (top left) Roll (red) and pitch (blue) of the aircraft; (middle left) horizontal cross-track swath for the DD grid. (top right), (middle right) The single-Doppler standard deviations as functions of the radar SNR. (bottom right) The radar SNR and (bottom left) the RMS error of the DD velocity field.

ATM-0742147. Additional support was provided by the FWF (Austrian Science Fund) Grant P24726-N27 (PI S. Serafin) to the University of Vienna. The data were collected through a NASA Grant EPSCoR-3412 (PIs B. Geerts, D. Leon, and J. Snider) to the University of Wyoming. The authors thank Dr. Leon from the

University of Wyoming, who was flight scientist on the UWKA for both flights, and would like to thank the UWKA crew for the planning and execution of the flights and data processing. The comments provided by the anonymous reviewers contributed substantially to improving the manuscript.

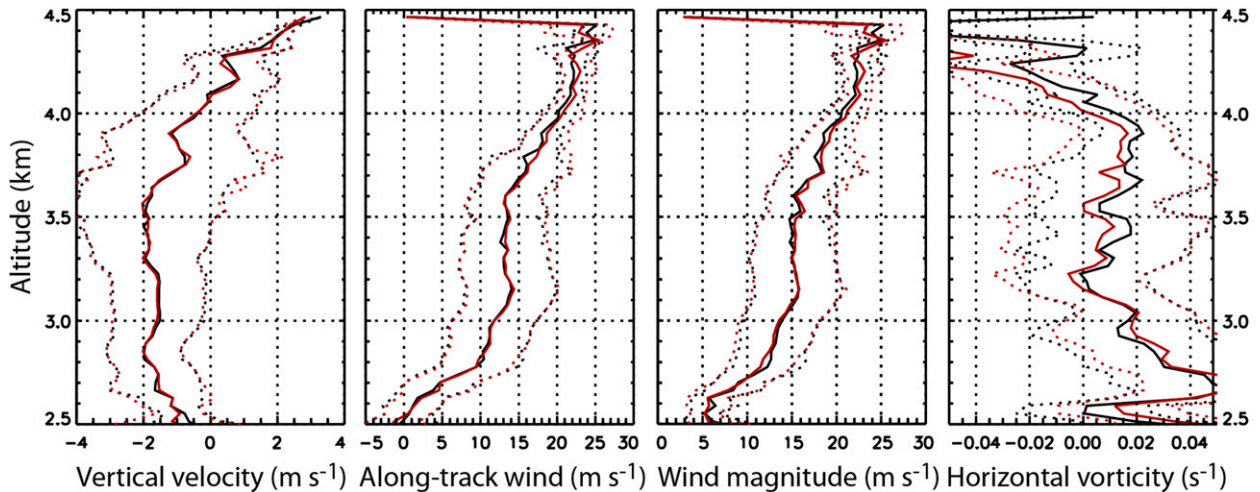


FIG. A2. The 26 Jan leg-5 variability of the mean dual-Doppler (resolution of about $30 \times 30 \text{ m}^2$) synthesized vertical profile of the winds due to errors in the assumed mean wind grid advection and vertical profile of the winds. Two error boundary cases are shown. Black curves indicate mean-wind grid advection and the crosswind guess are equal to the aircraft-measured mean winds. Red curves indicate no advection and 0 m s^{-1} crosswind guess. Dotted lines bracket two standard deviations.

APPENDIX

Dual-Doppler Error Analysis and Vertical Air Motion Uncertainty

a. Error analysis

Analysis of the DD errors is performed for all data segments presented in this study. One example is shown in Fig. A1. The variation in roll (top left) is responsible for the change in the cross-track swath (middle left). For this case, the maximum cross-track swath (horizontal displacement of the cross-track field of view) is about 150 m, which is acceptable for resolving spatial features of similar and larger scale. The aircraft roll also causes contamination, estimated to be less than 1 m s^{-1} , of the single-Doppler measurements from the cross-track wind. The variation in the pitch angle plays no significant role in the DD errors. The standard deviation in the Doppler velocity measurements from the two beams (top and middle right) results from the finite SNR of the radar return signals (bottom right). The SNR for most of the received power is above 12 dB, resulting in less than 1 m s^{-1} Doppler uncertainty. The absolute root-mean-square error from the DD synthesis is shown in the bottom-left panel. The DD mean error for this leg is on the order of $1\text{--}2 \text{ m s}^{-1}$. The maximum error encountered is larger mostly downstream of the boundary layer separation and in the border regions of the rotor because of the lack of data and/or low SNR.

Additional consideration is warranted for the errors in the DD synthesis caused by crosswind contamination and advection during the time the two beams illuminate

the target volumes. Depending on the distance from the radar to the target volume, the time between the two beams illuminating the same target is 2–10 s. We assume that during this time there is no appreciable change in the target. Also an assumption regarding the possible advection of the analyzed features is needed (Damiani and Haimov 2006). To investigate the effect of the advection and the error in the guess of the crosswind component, DD cases are processed with two extreme conditions: 1) where the aircraft-measured mean winds are used for the mean grid advection and the crosswind guess and 2) where there is no grid advection and the mean crosswind is 0 m s^{-1} . The difference in the retrieved 2D kinematics for these two cases provides an estimate of the expected maximum mean error. Processing both conditions for the 26 January leg-5 results in small differences in the 2D velocity components but considerably larger differences for the horizontal vorticity¹ (Fig. A2). This is to be expected given that the vorticity is affected more by the measurements' noise due to the computation of the spatial gradients. To reduce the error in the vorticity, we applied additional spatial averaging ($150 \times 90 \text{ m}^2$). The distortion in the spatial characteristics inside the rotor is also small (not shown). Therefore, while our 2D wind retrieval cannot be used to determine the exact shape, location, and velocity characteristics of the fine 2D structure inside the

¹ Note that $\eta = \partial u / \partial z - \partial w / \partial x$, where u (w) is the horizontal (vertical) wind, and z (x) is the vertical (horizontal) along the flight track axis.

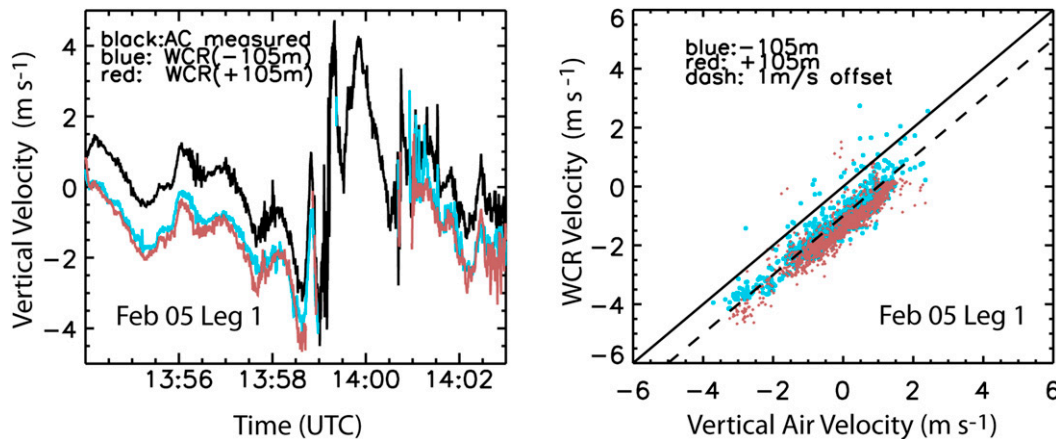


FIG. A3. Aircraft-measured (black) vertical air motion and radar Doppler measurements (red and blue) of (left) vertical particle motion and (right) regression fit for data during leg 1 on 5 Feb showing the presence of near 1 m s^{-1} bias in the radar Doppler velocity caused by particle terminal fall velocity. Note that, between 1359:00 and 1400:30 UTC, there were no radar data near the flight level.

rotor, the average characteristics of the rotor structure of several hundred meters or more is expected to be reasonably accurate.

For the cases presented in this paper, the overall error in the DD-synthesized 2D velocity field is on the order of 2 m s^{-1} , with the 5 February case having slightly lower uncertainty than the 26 January case.

b. Vertical air motion uncertainty

The DD synthesis provides the along-track horizontal velocity and vertical velocity components of the mean scatterers' motion for each 2D grid cell. To retrieve the 2D air motion, the particles' mean fall velocity must be removed. The DD horizontal component includes a negligible error as a result of contamination from the fall velocity; however, the error is larger for the vertical component of the air motion and could be of the same order as the actual vertical air motion.

The mean value of the fall velocities is estimated by using the aircraft-measured vertical velocity at the aircraft level and the radar Doppler measurements in the closest radar range gates ($\sim 100 \text{ m}$) above and below the aircraft. Combining the up and down beam measurements allows us to bracket the aircraft measurements at flight level but requires the assumption that the vertical air velocity is constant or changes linearly within the 200 m between the nearest up and down range gates. The averaged Doppler measurements from both beams represent the mean vertical air motion and particle mean fall velocity at the flight level. An illustration of the hydrometeor mean fall velocity estimate is shown in Fig. A3. An average fall velocity of about 1 m s^{-1} appears to be present in the Doppler measurements with a standard deviation of about 0.2 m s^{-1} .

In situ measurements from the mountain cap cloud on 5 February and in the rotor cloud on 26 January show that maximum particle dimensions were about 0.8 and 1.2 mm , respectively. On both days, particles appeared to be spherically shaped aggregates, possibly with some riming, although measured liquid water at flight level was always less than 0.1 g m^{-3} . No pristine crystals are seen in the data. Based on direct measurements and models of ice particle terminal velocity, an estimate of $0.75\text{--}1.0 \text{ m s}^{-1}$ for these larger particles is justified (Mitchell 1996). Therefore, a 1 m s^{-1} correction of mean particle fall speed has been applied to all Doppler data to allow better representation of the true vertical air velocity.

REFERENCES

- Armi, L., and G. J. Mayr, 2011: The descending stratified flow and internal hydraulic jump in the lee of the Sierras. *J. Appl. Meteor. Climatol.*, **50**, 1995–2011, doi:10.1175/JAMC-D-10-05005.1.
- Baines, P. G., 1995: *Topographic Effects in Stratified Flows*. Cambridge University Press, 489 pp.
- Brown, E. N., C. A. Friehe, and D. H. Lenschow, 1983: The use of pressure fluctuations on the nose of an aircraft for measuring air motion. *J. Climate Appl. Meteor.*, **22**, 171–180, doi:10.1175/1520-0450(1983)022<0171:TUOPFO>2.0.CO;2.
- Cohn, S. A., V. Grubišić, and W. O. J. Brown, 2011: Wind profiler observations of mountain waves and rotors during T-REX. *J. Appl. Meteor. Climatol.*, **50**, 826–843, doi:10.1175/2010JAMC2611.1.
- Comman, L. B., C. S. Morse, and G. Cuning, 1995: Real-time estimation of atmospheric turbulence severity from in-situ aircraft measurements. *J. Aircr.*, **32**, 171–177, doi:10.2514/3.46697.
- Damiani, R., and S. Haimov, 2006: A high-resolution dual-Doppler technique for fixed multi-antenna airborne radar. *IEEE Trans. Geosci. Remote Sens.*, **44**, 3475–3489, doi:10.1109/TGRS.2006.881745.

- Doyle, J. D., and D. R. Durran, 2002: The dynamics of mountain-wave-induced rotors. *J. Atmos. Sci.*, **59**, 186–201, doi:[10.1175/1520-0469\(2002\)059<0186:TDOMWI>2.0.CO;2](https://doi.org/10.1175/1520-0469(2002)059<0186:TDOMWI>2.0.CO;2).
- , and —, 2007: Rotor and subrotor dynamics in the lee of three-dimensional terrain. *J. Atmos. Sci.*, **64**, 4202–4221, doi:[10.1175/2007JAS2352.1](https://doi.org/10.1175/2007JAS2352.1).
- , V. Grubišić, W. O. J. Brown, S. F. J. DeWekker, A. Dörnbrack, Q. Jiang, S. D. Mayor, and M. Weissmann, 2009: Observations and numerical simulations of subrotor vortices during T-REX. *J. Atmos. Sci.*, **66**, 1229–1249, doi:[10.1175/2008JAS2933.1](https://doi.org/10.1175/2008JAS2933.1).
- Feng, X., 2001: Evaluation of the MacCready turbulence sensor. M.S. thesis, Dept. of Atmospheric Science, University of Wyoming, 81 pp.
- Gohm, A., and G. J. Mayr, 2005: Numerical and observational case-study of a deep Adriatic bora. *Quart. J. Roy. Meteor. Soc.*, **131**, 1363–1392, doi:[10.1256/qj.04.82](https://doi.org/10.1256/qj.04.82).
- , —, A. Fix, and A. Giez, 2008: On the onset of bora and the formation of rotors and jumps near a mountain gap. *Quart. J. Roy. Meteor. Soc.*, **134**, 21–46, doi:[10.1002/qj.206](https://doi.org/10.1002/qj.206).
- Grubišić, V., and Coauthors, 2008: The Terrain-Induced Rotor Experiment. *Bull. Amer. Meteor. Soc.*, **89**, 1513–1533, doi:[10.1175/2008BAMS2487.1](https://doi.org/10.1175/2008BAMS2487.1).
- , S. Serafin, L. Strauss, S. J. Haimov, J. R. French, and L. D. Oolman, 2015: Wave-induced boundary layer separation in the lee of the Medicine Bow Mountains. Part II: Numerical modeling. *J. Atmos. Sci.*, **72**, 4865–4884, doi:[10.1175/JAS-D-14-0381.1](https://doi.org/10.1175/JAS-D-14-0381.1).
- Hertenstein, R. F., 2009: The influence of inversions on rotors. *Mon. Wea. Rev.*, **137**, 433–446, doi:[10.1175/2008MWR2482.1](https://doi.org/10.1175/2008MWR2482.1).
- , and J. P. Kuettner, 2005: Rotor types associated with steep lee topography: Influence of the wind profile. *Tellus*, **57A**, 117–135, doi:[10.1111/j.1600-0870.2005.00099.x](https://doi.org/10.1111/j.1600-0870.2005.00099.x).
- Hill, M., R. Calhoun, H. J. S. Fernando, A. Wieser, A. Dörnbrack, M. Weissmann, G. Mayr, and R. Newsom, 2010: Coplanar Doppler lidar retrieval of rotors from T-REX. *J. Atmos. Sci.*, **67**, 713–729, doi:[10.1175/2009JAS3016.1](https://doi.org/10.1175/2009JAS3016.1).
- Jiang, Q., J. D. Doyle, S. Wang, and R. B. Smith, 2007: On boundary layer separation in the lee of mesoscale topography. *J. Atmos. Sci.*, **64**, 401–420, doi:[10.1175/JAS3848.1](https://doi.org/10.1175/JAS3848.1).
- Leon, D., and G. Vali, 1998: Retrieval of three-dimensional particle velocity from airborne Doppler radar data. *J. Atmos. Oceanic Technol.*, **15**, 860–870, doi:[10.1175/1520-0426\(1998\)015<0860:ROTDVP>2.0.CO;2](https://doi.org/10.1175/1520-0426(1998)015<0860:ROTDVP>2.0.CO;2).
- , —, and M. Lothon, 2006: Dual-Doppler analysis in a single plane from an airborne platform. *J. Atmos. Oceanic Technol.*, **23**, 3–22, doi:[10.1175/JTECH1820.1](https://doi.org/10.1175/JTECH1820.1).
- Lilly, D. K., 1978: A severe downslope windstorm and aircraft turbulence event induced by a mountain wave. *J. Atmos. Sci.*, **35**, 59–77, doi:[10.1175/1520-0469\(1978\)035<0059:ASDWAA>2.0.CO;2](https://doi.org/10.1175/1520-0469(1978)035<0059:ASDWAA>2.0.CO;2).
- MacCready, P. B., Jr., 1964: Standardization of gustiness values from aircraft. *J. Appl. Meteor.*, **3**, 439–449, doi:[10.1175/1520-0450\(1964\)003<0439:SOGVFA>2.0.CO;2](https://doi.org/10.1175/1520-0450(1964)003<0439:SOGVFA>2.0.CO;2).
- Mitchell, D. L., 1996: Use of mass- and area-dimensional power laws for determining precipitation particle terminal velocities. *J. Atmos. Sci.*, **53**, 1710–1723, doi:[10.1175/1520-0469\(1996\)053<1710:UOMAAD>2.0.CO;2](https://doi.org/10.1175/1520-0469(1996)053<1710:UOMAAD>2.0.CO;2).
- Nappo, C. J., 2002: *An Introduction to Atmospheric Gravity Waves*. Academic Press, 400 pp.
- Ozawa, H., K. Goto-Azuma, K. Iwanami, and R. M. Koerner, 1998: Cirriform rotor cloud observed on a Canadian Arctic ice cap. *Mon. Wea. Rev.*, **126**, 1741–1745, doi:[10.1175/1520-0493\(1998\)126<1741:POTMCR>2.0.CO;2](https://doi.org/10.1175/1520-0493(1998)126<1741:POTMCR>2.0.CO;2).
- Rodi, A., 2011: King of the air: The evolution and capabilities of Wyoming's observation aircraft. *Meteorological Technology International*, May, UKIP Media and Events, Surrey, United Kingdom, 44–47.
- , and P. A. Spyers-Duran, 1972: Analysis of time response of airborne temperature sensors. *J. Appl. Meteor.*, **11**, 554–556, doi:[10.1175/1520-0450\(1972\)011<0554:AOTROA>2.0.CO;2](https://doi.org/10.1175/1520-0450(1972)011<0554:AOTROA>2.0.CO;2).
- Sharman, R. D., L. B. Cornman, G. Meymaris, J. Pearson, and T. Farrar, 2014: Description and derived climatologies of automated in situ eddy-dissipation-rate reports of atmospheric turbulence. *J. Appl. Meteor. Climatol.*, **53**, 1416–1432, doi:[10.1175/JAMC-D-13-0329.1](https://doi.org/10.1175/JAMC-D-13-0329.1).
- Smith, R. B., 1979: The influence of mountains on the atmosphere. *Advances in Geophysics*, Vol. 21, Academic Press, 87–230.
- Strauss, L., S. Serafin, S. Haimov, and V. Grubišić, 2015: Turbulence in breaking mountain waves and atmospheric rotors from airborne in situ and Doppler radar measurements. *Quart. J. Roy. Meteor. Soc.*, doi:[10.1002/qj.2604](https://doi.org/10.1002/qj.2604), in press.
- Vosper, S. B., 2004: Inversion effects on mountain lee waves. *Quart. J. Roy. Meteor. Soc.*, **130**, 1723–1748, doi:[10.1256/qj.03.63](https://doi.org/10.1256/qj.03.63).
- Wendisch, M., and J. Brenguier, Eds., 2013: *Airborne Measurements for Environmental Research*. Wiley-VCH, 641 pp.